Chinese Chemical Letters 35 (2024) 109301

Contents lists available at ScienceDirect

Chinese Chemical Letters

journal homepage: www.elsevier.com/locate/cclet

Fe nanoclusters anchored in biomass waste-derived porous carbon nanosheets for high-performance supercapacitor

Yuchen Wang[a,b], Yaoyu Liu[a], Xiongfei Huang[a], Guanjie He[c,*], Kai Yan[a,*]

[a] Guangdong Provincial Key Laboratory of Environmental Pollution Control and Remediation Technology, School of Environmental Science and Engineering, Sun Yat-sen University, Guangzhou 510275, China
[b] Key Laboratory of Advanced Energy Materials Chemistry (Ministry of Education), Nankai University, Tianjin 300071, China
[c] Electrochemical Innovation Lab, Department of Chemical Engineering, University College London, London, WC1E 7JE, United Kingdom

ARTICLE INFO

Article history:
Received 6 August 2023
Revised 25 October 2023
Accepted 11 November 2023
Available online 15 November 2023

Keywords:
Fe nanoclusters
Biomass waste
Porous carbon nanosheets
Supercapacitor
Charge transfer

ABSTRACT

Metal-nanocluster materials have gradually become a promising electrode candidate for supercapacitor application. The high-efficient and rational architecture of these metal-nanocluster electrode materials with satisfied supercapacitive performance are full of challenges. Herein, Fe-nanocluster anchored porous carbon (FAPC) nanosheets were constructed through a facile and low-cost impregnation-activation strategy. Various characterization methods documented that FAPC nanosheets possessed a mesopore-dominated structure with large surface area and abundant Fe-N_4 active sites, which are crucial for supercapacitive energy storage. The optimal FAPC electrode exhibited a high specific capacitance of 378 F/g at a specific current of 1 A/g and an excellent rate capability (271 F/g at 10 A/g), which are comparable or even superior to that of most reported carbon candidates. Furthermore, the FAPC-based device achieved a desired specific energy of 14.8 Wh/kg at a specific power of 700 W/kg. This work opens a new avenue to design metal-nanocluster materials for high-performance biomass waste-based supercapacitors.

With the excessive exhaustion of fossil fuels, green energy storage technologies offer an eco-friendly and sustainable solution to alleviate the energy crisis and associated environmental problems [1]. Supercapacitor (SC) is a renewable energy storage device that can charge/discharge *via* ion adsorption/desorption and rapid reversible faradaic reactions on the electrode-electrolyte interface [2–4]. In general, the capacitance of electrode materials including the electrical double-layer capacitance and pseudocapacitance is highly dependent on their intrinsic electronic conductivity σ_e, which is governed by electron density n_e and electron mobility μ_e according to the equation of $\sigma_e = en_e\mu_e$ [5–8]. Therefore, dedicated manipulation of electronic structure is conducive to boosting the electron-driven activity of electrode materials to realize desired supercapacitive performance.

Single-atom materials (SAMs) with distinctive unsaturated electronic structure have been widely used in the catalytic research area [9–13]. These advanced nanomaterials are generally embedded in modified carbon materials to ensure the uniform distribution of metal atoms, accelerate the electronic transport between active sites and substrate, and eventually maximize the utilization of active sites [14–16]. Nevertheless, the low mass loading and insufficient active sites prevent their extensive application as standalone energy storage materials [17]. Recently, upsizing SAMs to metal-nanocluster materials with high electron cloud density is expected as a feasible way to achieve excellent supercapacitive performance. For instance, Joseph *et al.* [18] employed a hard template method to prepare highly-ordered porous carbon with CaF_2 nanoclusters as SC electrode materials. The incorporation of CaF_2 nanoclusters improved the charge transfer and prevented the staking of carbon, leading to a maximum specific capacitance of 182 F/g. Hong *et al.* [19] applied a hydrothermal-calcination method to obtain SnO_2 nanocluster wrapped carbon cloth composites for SC. The intimate coupling between carbon fibers and SnO_2 nanoclusters gave rise to a high specific capacitance of 197.7 F/g at 1 A/g. Up to date, albeit metal-nanocluster materials have gradually attracted more attention in SC application, the correlation between active sites and charge storage ability has not been elucidated to improve their supercapacitive performance. Moreover, since metal nanoclusters tend to agglomerate owing to their high surface energy, the carbon matrix is always controllable constructed through complicated procedures to stabilize these metal nanoclusters, leading to high cost and long time-consuming [20]. Under this circumstance, it is urgent to seek a facile and economical method

* Corresponding authors.
E-mail addresses: g.he@ucl.ac.uk (G. He), yank9@mail.sysu.edu.cn (K. Yan).

https://doi.org/10.1016/j.cclet.2023.109301
1001-8417/

to design metal-nanocluster based electrode materials for high-performance SC.

Herein, we proposed a facile and low-cost method to fabricate high-performance Fe-nanocluster anchored porous carbon (FAPC) nanosheets from *Ficus altissima* wastes for SC application. Comprehensive characterization techniques, such as transmission electron microscopy (TEM), aberration-corrected high-angle annular dark field scanning transmission electron microscopy (AC-HAADF-STEM) and X-ray adsorption fine structure spectroscopy (XAFS), were employed to probe the influence of foreign Fe source on the structural and chemical properties of FAPC. Subsequently, a series of electrochemical measurements and analyses were implemented to clarify the crucial role of Fe nanoclusters on specific capacitance, rate capability and charge storage mechanism. Additionally, the supercapacitive performance of an assembled FAPC-based SC was assessed to evaluate the potential for practical utilization. This work creates a new path to design metal-nanocluster electrode materials for high-performance biomass waste-based SC.

Fig. S1 (Supporting information) briefly illustrates the schematic diagram of the fabrication process for FAPC materials. Powders from *Ficus altissima* branch wastes were firstly impregnated in Fe salt solution to host Fe atoms in pores through physical absorption. N-doping was then realized by immersing and dispersing precursors in an ammonia solution containing urea. Electronegative N atoms on the frame of precursors could attract and anchor electropositive Fe atoms to form Fe-nanoclusters [21]. Finally, FAPC nanosheets were obtained *via* a traditional chemical activation method using potassium bicarbonate ($KHCO_3$) as green activating agents. The detailed synthetic process and characterization methods are articulated in Supporting information. Related experimental procedures are similar to those reported in our previous publications [22,23]. The morphologies of as-prepared FAPC were characterized by field-emission scanning electron microscopy (FE-SEM) and TEM. From FE-SEM images (Figs. 1a and d), it can be seen that both FAPC-0 and FAPC-10 exhibited distinct porous structure, which was mainly attributed to $KHCO_3$ activation [24]. The TEM image of FAPC-0 in Fig. 1b also revealed the formation of pore structure. Interestingly, the TEM image of FAPC-10 in Fig. 1e displayed the formation of the nanosheet structure. The morphological change may be owed to the intercalation of Fe-nanocluster into the carbon framework, which is beneficial for delaminating *Ficus altissima* precursors during the activation process. Subsequently, the high-resolution TEM (HR-TEM) images of FAPC (Figs. 1c and f) illustrated the long-range disordered structure, manifesting the amorphous nature of the materials. Furthermore, AC-HAADF-STEM image in Fig. 1g clearly identified Fe-nanocluster as bright dots. The corresponding energy-dispersive X-ray spectroscopy (EDS, Figs. 1h and i) unveiled the uniform distribution of Fe nanoclusters over the entire porous structure.

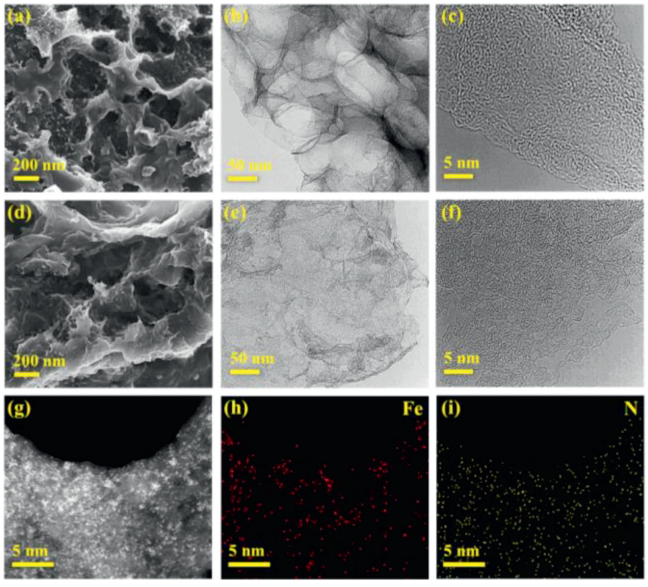

Fig. 1. Morphological characterization of FAPC materials. (a) FE-SEM, (b) TEM and (c) HR-TEM images of FAPC-0. (d) FE-SEM, (e) TEM and (f) HR-TEM images of FAPC-10. (g-i) AC-HAADF-STEM image and corresponding element mapping images of FAPC-10.

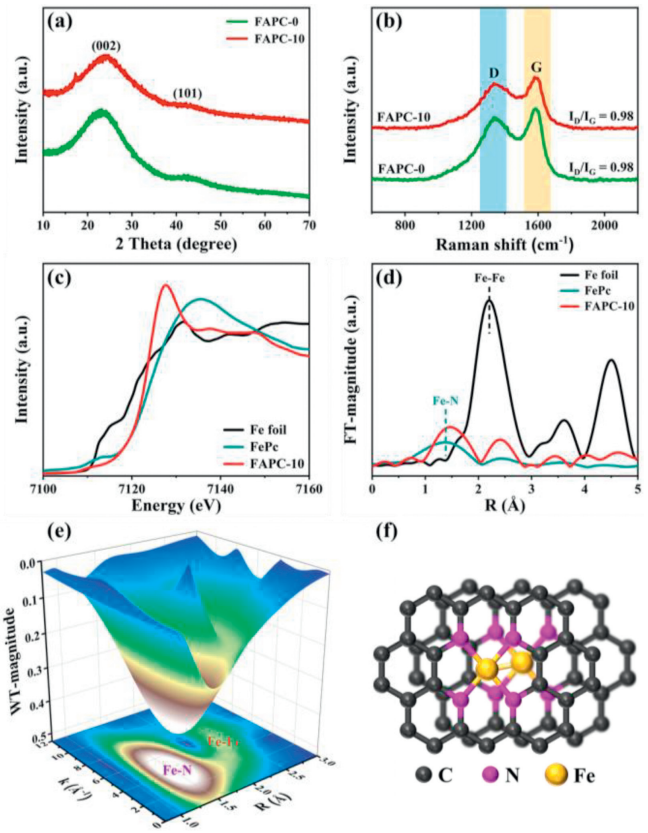

Fig. 2. Structural information and coordination environment of FAPC materials. (a) XRD patterns, (b) Raman spectra of FAPC-0 and FAPC-10. (c) Fe K-edge XANES spectra and (d) FT-EXAFS spectra of Fe foil, FePc, and FAPC-10. (e) WT-EXAFS spectrum and (f) the schematic structure of Fe-nanocluster sites of FAPC-10.

The powder X-ray diffraction (XRD) patterns of FAPC-0 and FAPC-10 (Fig. 2a) exhibited two broad peaks in the ranges of 20°−30° and 40°−50°, which were assigned to the (002) and (101) crystal planes of carbon, respectively [25]. It is noticeable that no other diffraction peaks for metallic Fe or Fe compounds are observed in the XRD pattern of FAPC-10. Raman spectra of the as-prepared FAPC in Fig. 2b displayed two prominent peaks at ~1340 and 1580 cm^{-1}, which can be assigned to the D band (sp^3) and G band (sp^2) of carbon species, respectively. The I_D/I_G values for two samples were calibrated as 0.98. Similar I_D/I_G values of both samples implied that the Fe decoration could not influence the crystallinity of FAPC [26]. Moreover, the porosity information of FAPC was clarified by N_2 adsorption-desorption isotherms. According to Fig. S2a (Supporting information), type I and type IV isotherm curves of FAPC-0 and FAPC-10 demonstrated micropore- and mesopore-dominated structure [27,28], respectively, which are confirmed by the corresponding pore size distribution (Fig. S2b in Supporting information). As summarized in Table S1 (Supporting information), the large surface area (1014.57 m^2/g) and total pore volume (1.05 cm^3/g) of FAPC-10 are advantageous for the expo-

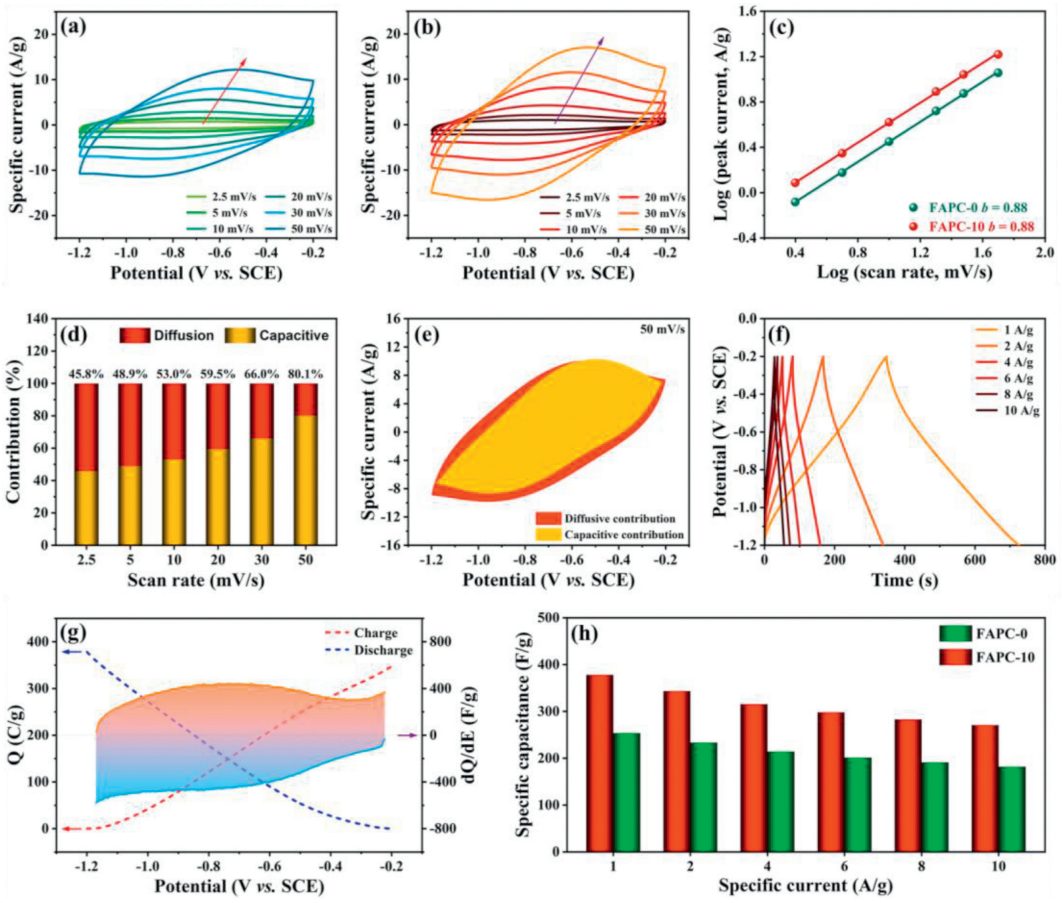

Fig. 3. Electrochemical performance of FAPC electrodes. CV curves of (a) FAPC-0 and (b) FAPC-10 at scan rates from 2.5 mV/s to 50 mV/s. (c) The *b*-value calculation with the reduction peak current and the scan rate for FAPC-0 and FAPC-10. (d) Charge storage mechanism analysis of FAPC-10. (e) Diffusive and capacitive contribution at a scan rate of 50 mV/s for FAPC-10. (f) GCD curves of FAPC-10 at specific currents from 1 A/g to 10 A/g. (g) The differential charge *versus* potential (d*Q*/d*E*) curve of FAPC-10 at a specific current of 1 A/g. (h) Specific capacitance values of FAPC-0 and FAPC-10 as a function of specific current.

sure of abundant active sites and the acceleration of electrolyte ion/reactant transport [29].

To decipher the coordination environment of Fe-nanocluster in FAPCs, XAFS technique was performed. Based on inductively coupled plasma mass spectrometry (ICP-MS, Table S2 in Supporting information) and elemental analytical results (Table S3 in Supporting information), the presence of C, N, O, and Fe elements with no extra contaminants was confirmed in FAPCs and the maximum Fe content was measured as ~0.55 wt%. Fig. 2c shows the Fe K-edge X-ray absorption near edge structure (XANES) of FAPC-10 and two reference samples of Fe foil and iron phthalocyanine (FePc). FAPC-10 exhibited an absorption edge nearly identical to that of FePc, suggesting that the Fe sites in FAPC-10 are mainly in +2 oxidation state. The corresponding Fourier-transformed extended X-ray absorption fine structure (FT-EXAFS) spectra in Fig. 2d indicated that the peak at 1.5 Å and 2.4 Å can be ascribed to the Fe-N bond and Fe-Fe bond, respectively. Afterward, the coordination environment of FAPC-10 is intuitively visualized in the wavelet-transformed EXAFS (WT-EXAFS) spectra (Fig. 2e). The center of maximum intensity at approximate 4.3 $Å^{-1}$ further confirmed the predominance of Fe-N bond and a weak intensity at 6.1 $Å^{-1}$ could be attributed to Fe-Fe bond. Moreover, after fitting the R space of FAPC-10 (Fig. S3 and Table S4 in Supporting information), the coordination number of Fe-N and Fe-Fe bonds were derived as 4.1 and 1.1, indicating the successful formation of Fe-N_4 active center and Fe nanoclusters, respectively [30]. Based on above measurements and theoretical results, an atomic structure model of FAPC-10 was established, which is plotted in Fig. 2f.

Figs. 3a and b shows cyclic voltammetry (CV) curves of FAPC at various scan rates. All CV curves displayed the symmetric shape with a pair of broad redox peaks, indicating that the electrochemical behaviors of FAPC include both electric double layer capacitive and pseudocapacitive processes. Compared with FAPC-0, FAPC-10 possessed redox peaks with greater specific currents, which were attributed to the transformation between $Fe(OH)_2$ and FeOOH [31]. Based on these CV curves, the charge storage mechanism of FAPC was clarified by employing the equation of $i = a\nu^b$ [32], where i is the cathodic peak current and ν is the scan rate. Theoretically, the *b*-value of 0.5 and 1.0 represent the diffusive and capacitive-controlled electrochemical process, respectively. As shown in Fig. 3c, the *b*-value of FAPC-0 and FAPC-10 was derived as 0.88, demonstrating that the charge storage process of FAPC was governed by fast capacitive reactions. Concretely, capacitive and diffusive contributions were distinguished quantitatively by applying the formula of $i = k_1\nu + k_2\nu^{0.5}$ [33]. For FAPC-10, the capacitive contribution was calculated as 45.8% at 2.5 mV/s. With the increase of the scan rate, the capacitive contribution increased gradually, reaching 80.1% at 50 mV/s (Fig. 3d). The same tendency was also observed for FAPC-0 (Fig. S4 in Supporting information). Intriguingly, the capacitive ratios of FAPC-10 at high scan rates were almost the same as that of FAPC-0, representing that the redox reaction of Fe-nanoclusters was prone to be pseudocapacitive at rapid charge/discharge modes. This phenomenon could be explained by fitted CV curves of FAPC-10 at 10 and 50 mV/s (Fig. 3e and Fig. S5 in Supporting information). When the scan rate was 50 mV/s, the capacitive contribution was distinctly observed

to be more concentrated in the area of redox peaks, which further confirmed the transition of charge storage mechanism along with the scan rate. Therefore, according to the above analysis, the charge storage mechanism on FAPC-10 can be expressed as follows (Eqs. 1 and 2):

$$\text{FAPC-10} + OH^- \leftrightarrow \text{FAPC-10}^+//OH^- + e^- \quad (1)$$

$$Fe(OH)_2 + OH^- \leftrightarrow FeOOH + H_2O + e^- \quad (2)$$

Analog to CV curves, galvanostatic charge/discharge (GCD) curves of FAPC in Fig. 3f and Fig. S6 (Supporting information) displayed typical capacitor behavior with high Coulombic efficiency. Fig. 3g shows the differential charge analysis of FAPC-10 at a specific current of 1 A/g. As expected, no sharp redox peak was observed during the charge/discharge process, further confirming the capacitive-controlled behavior of FAPC-10. Afterward, the average specific capacitance values of FAPC-0 and FAPC-10 were evaluated and compared in Fig. 3h according to their GCD curves. FAPC-10 achieved high specific capacitance of 378, 344, 316, 298, 283, 271 F/g at specific currents of 1, 2, 4, 6, 8, 10 A/g, respectively. These values were approximately 1.5 times compared to that of FAPC-0. Strikingly, the capacitance retention of FAPC-0 and FAPC-10 were all 72% from 1 A/g to 10 A/g, demonstrating that the incorporation of Fe-nanocluster could effectively enhance the specific capacitance of biomass waste-derived porous carbon without sacrificing rate capability. Moreover, the electrochemical impedance spectroscopy (EIS) technique was performed to understand the supercapacitive behavior of FAPC-10. Compared with the Nyquist plot of FAPC-0 (Fig. S7 in Supporting information), FAPC-10 possessed a relatively small and compressed semicircle, which indicated rapid electrochemical kinetics at the electrode/electrolyte interface [34]. Besides, the supercapacitive performance of FAPC materials were compared to optimize the exogenous Fe content in the fabrication process. From Fig. S8 (Supporting information), specific capacitance values of FAPC-0, FAPC-5, and FAPC-10 were 254, 308, and 378 F/g at a specific current of 1 A/g, denoting that the best Fe content for supercapacitive application was 10%. The maximum specific capacitance of 378 F/g could be comparable to recently reported biomass-derived porous carbon (Table S5 in Supporting information).

For practical application, FAPC-10 was assembled with commercial activated carbon YP-80F as an asymmetric SC. Considering the working potential of FAPC-10, YP-80F was used as a positive electrode in the SC. Fig. 4a illustrates CV curves of the assembled SC with different voltage windows at a scan rate of 10 mV/s. It is clearly observed that the irreversible oxygen evolution current was increased sharply after 1.4 V. Thus the appropriate working voltage was determined as 1.4 V to maximize the specific energy of SC. The supercapacitive performance of the SC was studied by CV and GCD curves at different charge/discharge rates. From Fig. 4b, all CV curves exhibited typical pseudocapacitive and electric double-layer capacitive behaviors within low- and high-voltage range, respectively, giving rise to the symmetric shapes. Accordingly, GCD curves in Fig. 4c displayed similar electrochemical behaviors. Subsequently, specific capacitance values of the SC were calculated from these GCD curves (Fig. S9 in Supporting information). The maximum value was achieved as 54 F/g at a specific current of 1 A/g. When the specific current was elevated to 10 A/g, the SC still maintained 45 F/g with 83% retention, presenting a remarkable rate capability. Subsequently, the Ragone plot in Fig. 4d visualized the operating power-energy performance of the SC in this work. The FAPC-10 based asymmetric SC reached a large specific energy of 14.8 Wh/kg at a specific power of 700 W/kg, which is comparable to those of biomass waste-derived porous carbon-based SC, such as pine nut shell-based SC (11.9 Wh/kg at 463.6 W/kg) [35],

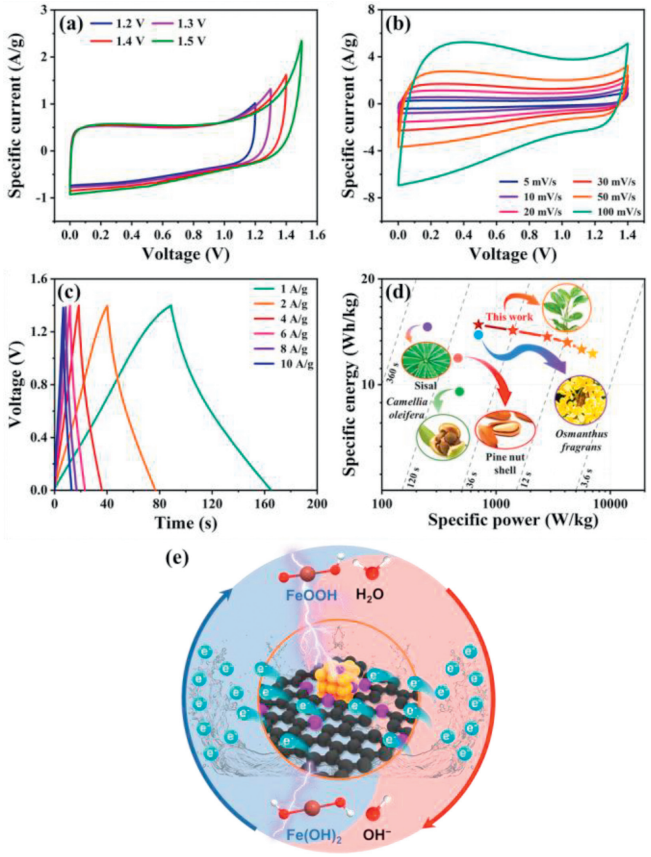

Fig. 4. Electrochemical performance of the FAPC-10 based asymmetric SC. (a) CV curves with different voltage windows at a scan rate of 10 mV/s. (b) CV curves at scan rates from 5 mV/s to 100 mV/s. (c) GCD curves at specific currents from 1 A/g to 10 A/g. (d) Ragone plot. (e) The proposed mechanism for efficient supercapacitive energy storage on Fe nanoclusters in FAPC-10.

Camellia oleifera-based SC (9.55 Wh/kg at 478 W/kg) [36], *Osmanthus fragrans*-based SC (13.86 Wh/kg at 700 W/kg) [37], and sisal-based SC (14.6 Wh/kg at 250 W/kg) [38]. In addition, the capacitance retention of the asymmetric SC remained 78% after 5000 cycles (Fig. S10 in Supporting information), indicating a satisfied cycling stability.

Based on the supercapacitive performance evaluation of FAPC-0 and FAPC-10, FAPC-10 exhibited excellent charge storage ability, which are attributed to the combined contribution of large surface area, high-concentration Fe-N_4 active center and mesopore-dominated structure. More importantly, the introduction of Fe nanoclusters not only provide substantial pesudocapacitance, but also promotes the charge transfer processes between $Fe(OH)_2$ and FeOOH (Fig. 4e). Consequently, the FAPC-10 achieved a maximum specific capacitance of 378 F/g.

In summary, we have successfully fabricated FAPC nanosheets from *Ficus altissima* wastes *via* a facile impregnation-activation method for SC application. The maximum specific capacitance of FAPC-10 was achieved as 378 F/g, which was almost 50% higher than that of pristine FAPC-0. Moreover, FAPC-10 based asymmetric SC reached a high specific energy of 14.8 Wh/kg at a specific power of 700 W/kg. The outstanding performance of FAPC-10 is mainly attributed to the following features: (1) Large surface area of the porous nanosheet structure offer abundant ion adsorption/desorption sites for double-layer capacitance. (2) Nitrogen-anchored Fe nanoclusters with substantial Fe-N_4 active sites provide high pesudocapacitance and boost the charge transfer kinetics. (3) Mesopore-dominated porous structure guarantees fast ion/reactant transport to enhance the utilization of active sites dur-

ing charge/discharge processes. This work provides a useful guidance for rational design of high-performance metal-nanocluster electrode materials for biomass waste-based SC.

Declaration of competing interest

The authors declare that they have no known competing financial interests or personal relationships that could have appeared to influence the work reported in this paper.

Acknowledgments

This work was supported by the National Key R&D Program of China (No. 2023YFC3905804), the National Natural Science Foundation of China (Nos. 22078374, 22378434, and 22309210), the National Ten Thousand Talent Plan, the Key Realm Research and Development Program of Guangdong Province (No. 2020B0202080001), Science and Technology Planning Project of Guangdong Province, China (No. 2021B1212040008), Guangdong Basic and Applied Basic Research Foundation (No. 2022A1515011150), the Scientific and Technological Planning Project of Guangzhou (No. 202206010145), Fundamental Research Funds for the Central Universities, Sun Yat-sen University (No. 23qnpy85).

Supplementary materials

Supplementary material associated with this article can be found, in the online version, at doi:10.1016/j.cclet.2023.109301.

References

[1] H. Tao, Q. Fan, T. Ma, et al., Prog. Mater. Sci. 111 (2020) 100637.
[2] A.C. Forse, C. Merlet, J.M. Griffin, C.P. Grey, J. Am. Chem. Soc. 138 (2016) 5731–5744.
[3] M. Salanne, B. Rotenberg, K. Naoi, et al., Nat. Energy 1 (2016) 16070.
[4] S. Li, Z. Yang, M. Wu, et al., Energy Environ. Mater. 5 (2022) 1238–1250.
[5] C.C. Chen, J. Maier, Nat. Energy 3 (2018) 102–108.
[6] L. Zhang, D. Shi, T. Liu, et al., Mater. Today 25 (2019) 35–65.
[7] M. Papac, V. Stevanović, A. Zakutayev, R. O'Hayre, Nat. Mater. 20 (2021) 301–313.
[8] A.G. Kelly, D. O'Suilleabhain, C. Gabbett, J.N. Coleman, Nat. Rev. Mater. 7 (2022) 217–234.
[9] L. Liu, A. Corma, Chem. Rev. 118 (2018) 4981–5079.
[10] Y. Wang, Y. Qu, B. Qu, et al., Adv. Mater. 33 (2021) 2105482.
[11] L. Zhao, J. Bian, X. Zhang, et al., Adv. Mater. 34 (2022) 2205303.
[12] C. Zhai, Y. Chen, X. Huang, et al., Environ. Funct. Mater. 1 (2022) 219–229.
[13] A.Y. Zha, Q.B. Zha, Z. Li, et al., Rare Met. 42 (2023) 1274–1282.
[14] Z. Chen, S. Mitchell, E. Vorobyeva, et al., Adv. Funct. Mater. 27 (2017) 1605785.
[15] Y. Peng, B. Lu, S. Chen, Adv. Mater. 30 (2018) 1801995.
[16] A. Han, B. Wang, A. Kumar, et al., Small Methods 3 (2019) 1800471.
[17] P. Wang, D. Zhao, L. Yin, Energy Environ. Sci. 14 (2021) 1794–1834.
[18] S. Joseph, J.M. Lee, M.R. Benzigar, et al., Carbon 180 (2021) 101–109.
[19] X. Hong, S. Li, R. Wang, J. Fu, J. Alloys Compd. 775 (2019) 15–21.
[20] P. Yin, X. Luo, Y. Ma, et al., Nat. Commun. 12 (2021) 3135.
[21] J.C. Li, Z.Q. Yang, D.M. Tang, et al., NPG Asia Mater. 10 (2018) e461-e461.
[22] Y. Wang, Z. Chen, M. Zhang, et al., Green Energy Environ. 7 (2022) 1053–1061.
[23] Y. Wang, Y. Liu, A. Ejaz, K. Yan, Chin. Chem. Lett. 34 (2023) 107538.
[24] J. Deng, T. Xiong, F. Xu, et al., Green Chem. 17 (2015) 4053–4060.
[25] H. Yang, X. Chen, W.T. Chen, et al., ACS Nano 13 (2019) 8087–8098.
[26] Y. Liu, B. Huang, X. Zhang, et al., J. Power Sources 412 (2019) 125–133.
[27] H. Peng, B. Yao, X. Wei, et al., Adv. Energy Mater. 9 (2019) 1803665.
[28] J. Guo, J. Xu, X. Xiao, et al., Green Chem. 24 (2022) 8827–8839.
[29] L. Borchardt, M. Oschatz, S. Kaskel, Mater. Horiz. 1 (2014) 157–168.
[30] M. Liu, J. Lee, T.C. Yang, et al., Small Methods 5 (2021) 2001165.
[31] K.A. Owusu, L. Qu, J. Li, et al., Nat. Commun. 8 (2017) 14264.
[32] Y. Wang, Y. Liu, M. Zhang, et al., Sci. China Mater. 65 (2022) 1805–1813.
[33] V. Augustyn, P. Simon, B. Dunn, Energy Environ. Sci. 7 (2014) 1597–1614.
[34] C. Leng, Z. Zhao, Y. Song, et al., Nano-Micro Lett. 13 (2021) 8.
[35] L. Guan, L. Pan, T. Peng, et al., ACS Sustain. Chem. Eng. 7 (2019) 8405–8412.
[36] X. Bo, K. Xiang, Y. Zhang, et al., J. Energy Chem. 39 (2019) 1–7.
[37] J. Li, Y. Zou, C. Xiang, et al., J. Energy Storage 42 (2021) 103017.
[38] M. Li, H. Xiao, T. Zhang, et al., ACS Sustain. Chem. Eng. 7 (2019) 4716–4723.